

ORIGINAL ARTICLE

REEP6 mediates trafficking of a subset of Clathrin-coated vesicles and is critical for rod photoreceptor function and survival

Shobi Veleri^{1,†}, Jacob Nellisery¹, Bibhudatta Mishra^{1,‡},
Souparnika H. Manjunath¹, Matthew J. Brooks¹, Lijin Dong²,
Kunio Nagashima³, Haohua Qian⁴, Chun Gao⁵, Yuri V. Sergeev⁶,
Xiu-Feng Huang⁷, Jia Qu⁷, Fan Lu⁷, Artur V. Cideciyan⁸, Tiansen Li¹,
Zi-Bing Jin⁷, Robert N. Fariss⁵, Rinki Ratnapriya¹, Samuel G. Jacobson⁸ and
Anand Swaroop^{1,*}

¹Neurobiology Neurodegeneration and Repair Laboratory, ²Genetic Engineering Core, National Eye Institute, National Institutes of Health, Bethesda, MD 20892, USA, ³Frederick National Laboratory for Cancer Research, Frederick, MD 21701, USA, ⁴Visual Function Core, ⁵Biological Imaging Core, ⁶Ophthalmic Genetics and Visual Function Branch, National Eye Institute, National Institutes of Health, Bethesda, MD 20892, USA, ⁷The Eye Hospital of Wenzhou Medical University, Wenzhou 325027, China and ⁸Scheie Eye Institute, Department of Ophthalmology, Perelman School of Medicine, University of Pennsylvania, Philadelphia, PA 19104, USA

*To whom correspondence should be addressed. Tel: 301 435 5754; Fax: 301 480 9917; Email: swaroopa@nei.nih.gov

Abstract

In retinal photoreceptors, vectorial transport of cargo is critical for transduction of visual signals, and defects in intracellular trafficking can lead to photoreceptor degeneration and vision impairment. Molecular signatures associated with routing of transport vesicles in photoreceptors are poorly understood. We previously reported the identification of a novel rod photoreceptor specific isoform of Receptor Expression Enhancing Protein (REEP) 6, which belongs to a family of proteins involved in intracellular transport of receptors to the plasma membrane. Here we show that loss of REEP6 in mice (*Reep6*^{-/-}) results in progressive retinal degeneration. Rod photoreceptor dysfunction is observed in *Reep6*^{-/-} mice as early as one month of age and associated with aberrant accumulation of vacuole-like structures at the apical inner segment and reduction in selected rod phototransduction proteins. We demonstrate that REEP6 is detected in a subset of Clathrin-coated vesicles and interacts with the t-SNARE, Syntaxin3. In concordance with the rod degeneration phenotype in *Reep6*^{-/-} mice, whole exome sequencing identified homozygous REEP6-E75K mutation in two retinitis pigmentosa families of different ethnicities.

[†]Present address: Biochemistry and Molecular Mechanisms Laboratory, Agro-processing Technology Division, National Institute for Interdisciplinary Science and Technology, Council of Scientific and Industrial Research, Thiruvananthapuram, Kerala 695019, India.

[‡]Present address: Department of Ophthalmology and Visual Sciences, Johns Hopkins University School of Medicine, Baltimore, MD 21231, USA.

Received: November 30, 2016. Revised: March 8, 2017. Accepted: March 16, 2017

© The Author 2017. Published by Oxford University Press.

This is an Open Access article distributed under the terms of the Creative Commons Attribution Non-Commercial License (<http://creativecommons.org/licenses/by-nc/4.0/>), which permits non-commercial re-use, distribution, and reproduction in any medium, provided the original work is properly cited. For commercial re-use, please contact journals.permissions@oup.com

Our studies suggest a critical function of REEP6 in trafficking of cargo via a subset of Clathrin-coated vesicles to selected membrane sites in retinal rod photoreceptors.

Introduction

The photoreceptors in the vertebrate retina have evolved for efficient capture and transmission of visual signals. The rod photoreceptors have a very high sensitivity to light and can detect a single photon but have a slow response time, whereas cones show a faster response over a broad range of light intensity, mediate color vision and exhibit complex synaptic connectivity (1,2). To mediate their photoresponse, rod and cone photoreceptors have distinct topology of outer segment discs and of ribbon synapses. Despite the importance of cones for daylight vision, the acquisition of rod dominance was a key event during early mammalian evolution for energy efficiency (3) and/or to exploit a scotopic niche (4). The primate retina possesses a unique cone-only central fovea for high visual acuity and a distinct spatial distribution of the more populous rod cells (5). Dysfunction and/or degeneration of rod photoreceptors are early events in a majority of retinal and macular degenerative diseases (6,7).

The photoreceptors are polarized post-mitotic sensory neurons, with high energy requirements to maintain a depolarized state in the dark, for periodic renewal of outer segment discs, and light-driven transduction of visual signals at ribbon synapses (1). Despite remarkable similarity, rods and cones have different demands associated with membrane disc renewal and synaptic transmission (2,8,9). Targeted delivery of proteins and lipids to distinct membranes and organelles is essential for accomplishing photoreceptor functions, and defects in intracellular transport, such as misrouting of specific molecules, are associated with photoreceptor degeneration (10–17). Three coat complexes (Clathrin, COPI and COPII) facilitate intracellular trafficking of vesicles, which carry necessary information for delivering cargos to distinct target compartments (18). The docking and fusion of transport vesicles are mediated by specialized membrane-associated proteins, including SNAREs (19–22). Though transport defects are established as a major pathway leading to cell death, we have limited understanding of precise molecular mechanisms that target distinct transport vesicles to specific membrane sites in photoreceptors.

The quest to identify accessory factors that can promote the targeting of odorant receptors to the cell surface led to the discovery of Receptor Expression Enhancing Proteins (REEPs) (23), which are believed to be involved in intracellular trafficking by controlling cargo capacity at the endoplasmic reticulum (ER) (24). Mutations in REEP1 result in hereditary spastic paraplegia (25) by defective shaping of the ER tubules (26). REEPs have also been implicated in formation of the ER network and restructuring (27–29). The mammalian photoreceptors are the ideal neurons for evaluating vesicle trafficking because of their polarized morphology, high degree of compartmentalization, and their extraordinary rates of membrane synthesis and turnover. We had identified a novel isoform of REEP6, which includes an additional 27 amino acid residues compared to the previously reported isoform and is specifically expressed in rod photoreceptors (30,31). The expression of rod-specific REEP6 is regulated by the Maf-family leucine zipper transcription factor NRL that determines rod cell fate and differentiation (32). *In vivo* shRNA-knockdown of *Reep6* resulted in rod cell death (31). We therefore hypothesized that REEP6 is a critical mediator of intracellular vesicular transport in rod photoreceptors. Here, we demonstrate

that loss of *Reep6* results in photoreceptor dysfunction and death because of its role in trafficking of a subset of Clathrin-coated vesicles to membrane sites that likely include Syntaxin3 (STX3). We also identify a missense mutation (E75K) in REEP6 in two families with retinitis pigmentosa (RP) of African and East Asian ethnicity, further highlighting its crucial role in functional maintenance and survival of rod photoreceptors.

Results

Deletion of *Reep6* in mice results in progressive rod dysfunction

Using homologous recombination in mouse embryonic stem cells, we replaced most of the coding region (exon 2 to exon 4) of *Reep6* with the β -gal reporter sequence and a neomycin selection cassette (Fig. 1A). The mice homozygous for the targeted allele (*Reep6*^{-/-}) lacked the transcript (Fig. 1B) and protein (Fig. 1C). *Reep6*^{-/-} mice were viable and showed no obvious morphological defects; however, the *Reep6*^{-/-} males were sterile.

To further examine whether loss of REEP6 affected visual function, we recorded electroretinograms (ERGs) at various stimulus intensities under dark- and light-adapted conditions to test rod and cone responses, respectively. One-month old *Reep6*^{-/-} mice showed a reduced rod ERG compared to the controls (Fig. 1D); amplitudes of the scotopic *a*-wave (generated by rod photoreceptors) and the *b*-wave [generated mostly by bipolar cells that are post-synaptic to rod photoreceptors and possibly from Muller cells (33)] were abnormally decreased. Kinetic analysis of the *b*-wave in *Reep6*^{-/-} mice showed a slower response compared to the WT, especially in the rising phase (data not shown), implying potential defects in rod phototransduction and/or photoreceptor to bipolar cell neurotransmission. Scotopic response of *Reep6*^{-/-} retina declined further at three months and was almost undetectable by 12 months (Fig. 1D; Supplementary Material, Fig. S1). In contrast, the photopic response (generated by the cone photoreceptors) showed a decrease only by age 12 months in *Reep6*^{-/-} mice (Fig. 1E).

Reep6^{-/-} rod photoreceptors reveal accumulation of vacuoles

To understand the cellular basis of the early reduction in rod ERGs, we examined retinal histology of *Reep6*^{-/-} mice. The *Reep6*^{-/-} retina showed overt degeneration of photoreceptors as early as 2 months of age, and by 3 months, the outer nuclear layer (ONL) had a column of ~8 nuclei compared to 11–12 nuclei in the wild-type (WT) (Fig. 2A). The outer segments of photoreceptors in *Reep6*^{-/-} retina were shorter by 3 months and almost undetectable by 6 months (data not shown). At 12 months, the photoreceptors in *Reep6*^{-/-} retina had only 1–2 layers of photoreceptor nuclei with short inner segments. The photoreceptor degeneration was complete by 18 months (data not shown).

Ultrastructure analysis using electron microscopy of the P17 *Reep6*^{-/-} retina (before overt degeneration is detected) showed an accumulation of vacuole-like structures (indicated by arrows in Fig. 2B) at the apical inner segment.

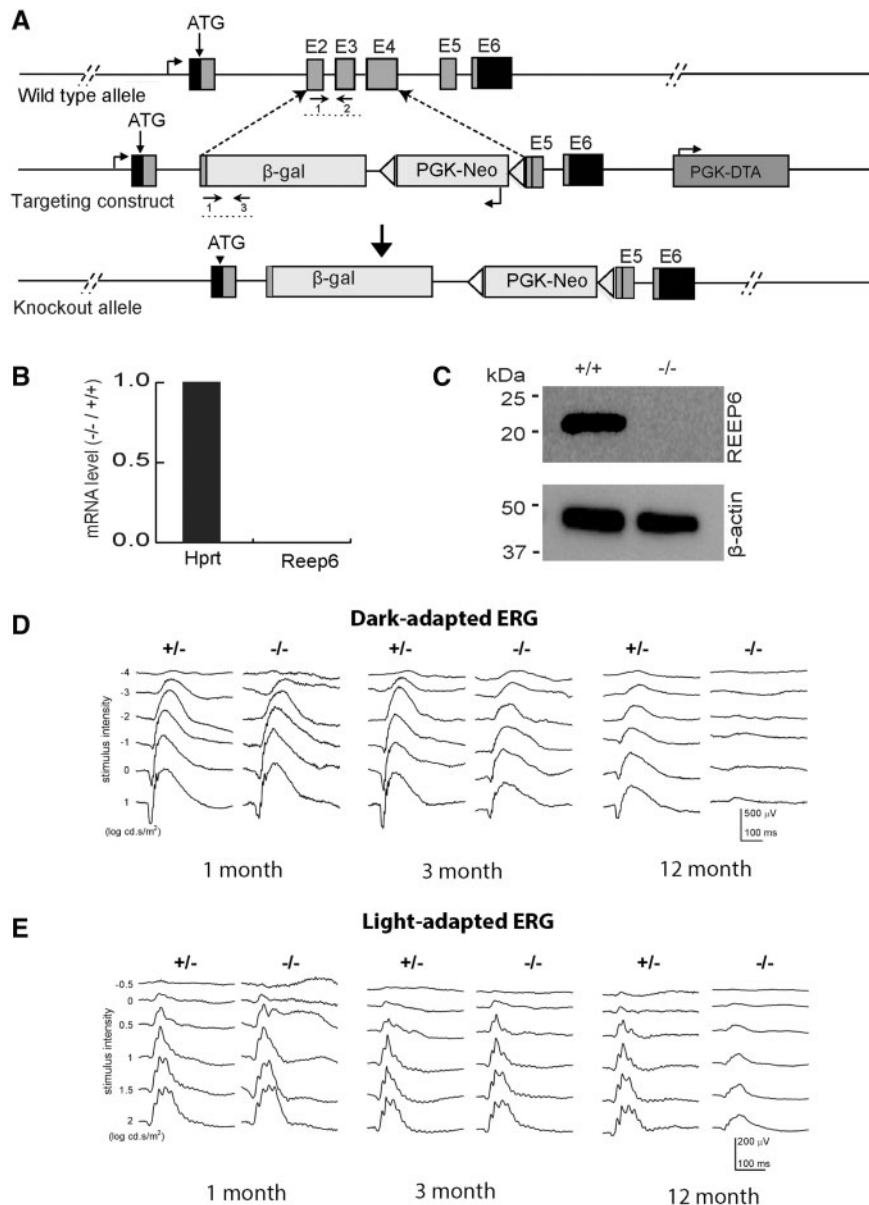


Figure 1. Targeted disruption of *Reep6* in mice. (A) Strategy for targeting *Reep6*. WT locus is shown at top. Grey boxes indicate exons (1–6). Arrows below the E2/E3 exons and β -gal boxes represent the primers used for screening/genotyping. The schematic of the targeting construct is shown in the middle and the knock out locus is shown at the bottom. (B) Expression profile of mRNA transcripts collected from WT and *Reep6*^{-/-} retinae, quantified by RT-qPCR using exon-specific Taqman probes. *Hprt* primers were used as a control. (C) Immunoblot of protein extracts from WT and *Reep6*^{-/-} mouse retina (P30). The REEP6 antibody detects 23 kDa protein, which is absent in the *Reep6*^{-/-} mice. (D–E) ERG traces at increasing light intensities from dark-adapted (D) and light-adapted (E) *Reep6*^{+/-} heterozygous (+/-) and *Reep6*^{-/-} (-/-) mice at 1 month, 3 months and 12 months of age. The amplitudes of the scotopic a-wave and the b-wave decrease significantly in *Reep6*^{-/-} mice.

Expression of selected rod genes/proteins is reduced in *Reep6*^{-/-} retina

We generated retinal gene expression profiles using RNA-seq to elucidate pathways impacted by the loss of *Reep6* (Supplementary Material, Fig. S2). We focused on early stages [postnatal day (P)9 and P21] before the onset of degeneration. While only 23 genes showed altered transcript levels at P9 (Supplementary Material, Table S1), we identified 94 differentially expressed genes (>2-fold change, adjusted FDR *P*-value <5%; Supplementary Material, Table S2A) in P21 *Reep6*^{-/-} retina. Seven-fold higher expression of glial fibrillary acidic protein (*Gfap*), a hallmark of gliosis, is consistent with retinal stress. In addition, genes involved in immune response and oxidative stress response demonstrated higher

expression in P21 *Reep6*^{-/-} retina (Supplementary Material, Table S2B). As two rod transcription factor genes, *Nrl* and *Ahr*, showed reduced expression levels, we specifically examined the expression of genes associated with phototransduction and synaptic function. Interestingly, we observed 30–50% decrease in the expression of almost all rod phototransduction genes (Supplementary Material, Table S3), whereas cone genes (except *Gnb3*) did not show significant change.

Guided by these observations, we evaluated the expression of phototransduction proteins in 1-month-old *Reep6*^{-/-} retina by immunofluorescent staining and immunoblot analysis (Fig. 3A and B). We observed similar rhodopsin protein levels in the WT and *Reep6*^{-/-} retina. Notably, immunoreactivity for rod cyclic nucleotide gated channel β 1 (CNGB1), cytoplasmic glutamic acid-

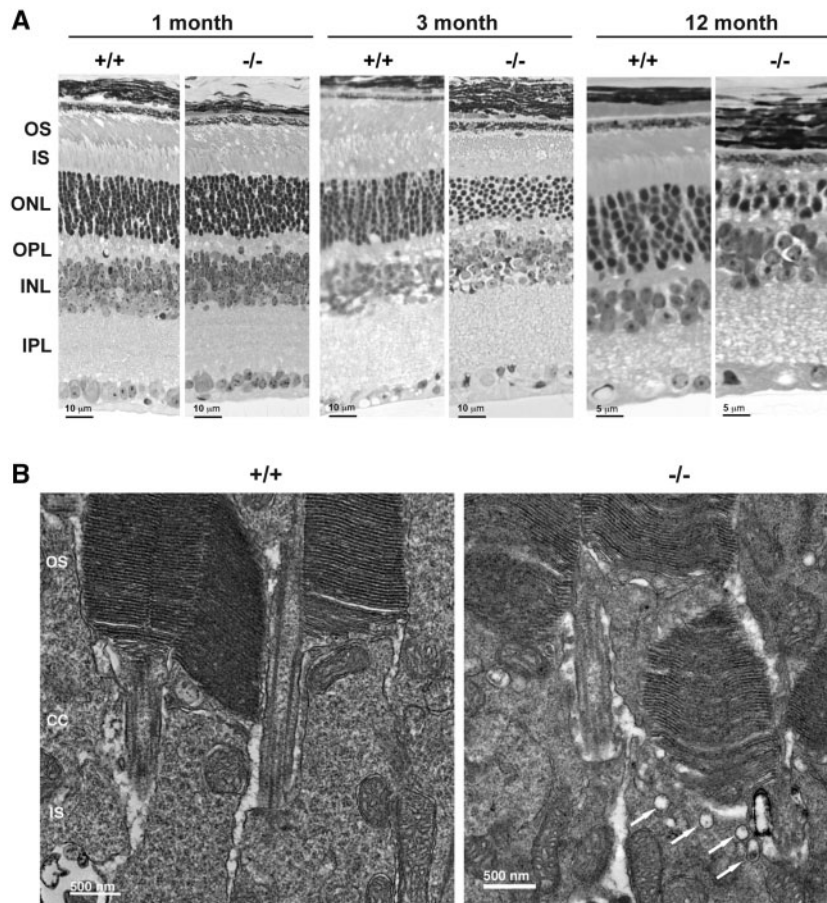


Figure 2. Photoreceptor degeneration in the retinae of *Reep6*^{-/-} is associated with accumulation of vacuoles in IS-OS junction. (A) Hematoxylin and eosin (HE) staining of retinae from 1, 3 and 12-month-old WT (+/+) and *Reep6* KO (-/-) mice. *Reep6*^{-/-} retinae showed loss of cells in the outer nuclear layer as early as 3 months of age. (B) Electron micrographs of P18 retina from WT (+/+) and *Reep6*^{-/-} (-/-) mice showing accumulation of vacuolar structures at the apical inner segment (arrows in Fig. 3B). OS, outer segment; CC, connecting cilium; IS, inner segment; ONL, outer nuclear layer; INL, inner nuclear layer; IPL, inner plexiform layer; OPL, outer plexiform layer.

proline-rich polypeptide (GARP), and transducin- α (GNAT1) was reduced in *Reep6*^{-/-} retina (Fig. 3A and B). AIP1, a chaperone of phosphodiesterase 6 (PDE6), was also decreased, but not δ subunit of PDE6 (PDE6D), in the retina of *Reep6*^{-/-} mice (Fig. 3B).

REEP6 is present in a subset of Clathrin-coated vesicles

A phenotype similar to that observed in *Reep6*^{-/-} retina had been reported in the retina of mice with defective vesicle trafficking (34). We therefore hypothesized that aberrant trafficking of phototransduction proteins in the absence of REEP6 may lead to their degradation by proteasome, as demonstrated in previous studies (35), and result in photoreceptor cell death. To gain further insights, we performed mass-spectrometry analysis of anti-REEP6 immunoprecipitated proteins from mouse retina. Among the proteins with minimum of two peptides, Clathrin Heavy Chain (CHC) was identified only in anti-REEP6 samples and not in IgG controls (two independent experiments) and selected for further studies because of its established role in vesicle trafficking. We then purified vesicle fractions from bovine retina extracts (Fig. 4A) to examine whether REEP6 is associated with trafficking of Clathrin-mediated vesicle transport. During fractionation, REEP6 was enriched in fractions containing vesicles, as identified by anti-Clathrin and anti- β -COPI, but not with

endoplasmic reticulum (anti-PDI) and nuclear (anti-CREB) markers (Fig. 4B). Other vesicle membrane proteins, SNAP25 and SV2 were also enriched along with REEP6 in the purified fraction (Fig. 4B). As predicted, the cytoplasmic domain of GARP (a soluble protein not participating in the secretory pathway) did not co-purify with REEP6-containing vesicles.

To further examine the association of REEP6 and Clathrin, we performed co-immunoprecipitation experiments. Anti-REEP6 antibody was able to immunoprecipitate Clathrin from the vesicle fraction of bovine retina (Fig. 4C, upper panel). In concordance, REEP6 protein was clearly evident in immunoblots of anti-Clathrin immunoprecipitate from mouse retinal extracts (Fig. 4C, lower panel). We then performed immuno-electron microscopy (EM) of vesicles isolated from bovine retina extracts using anti-REEP6 antibody. REEP6 gold particles were detected on a subset of vesicles that exhibited triskelion structure characteristic of Clathrin-coated vesicles (Fig. 4D).

To investigate co-localization of REEP6 and Clathrin, we did high resolution immunofluorescence microscopy using adult mouse retina sections. As reported previously (30,31), REEP6 labeling was evident throughout the rod photoreceptor with intense labeling in the outer plexiform layer (OPL) associated with spherules (rod-specific pre-synaptic morphology) (Fig. 4E, upper panel). Clathrin is ubiquitously expressed in rods but is also present at high levels in plexiform layers of the retina (Fig. 4E,

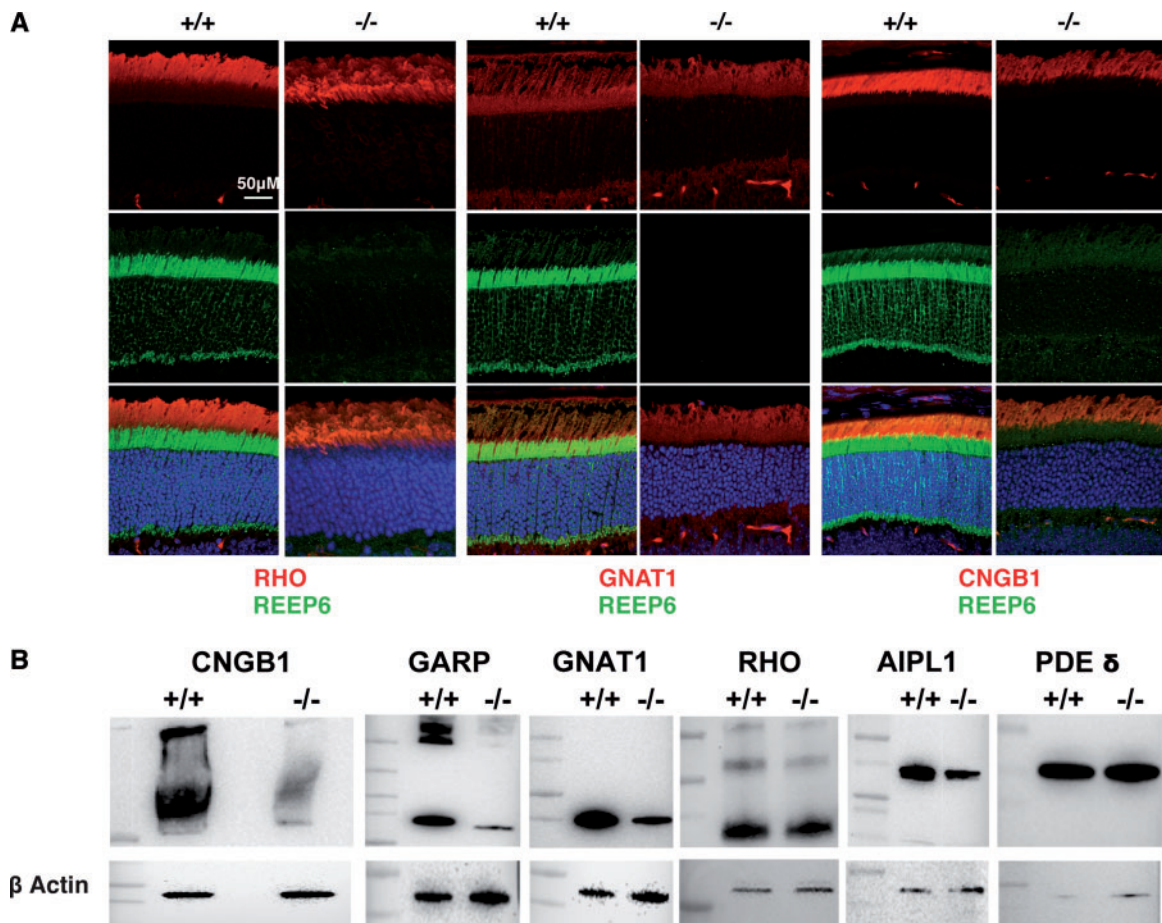


Figure 3. A subset of rod phototransduction proteins are reduced in *Reep6*^{-/-} retina. (A) Immunostaining of retinal sections from 4-week-old WT (+/+) and *Reep6*^{-/-} (-/-) mice with specific antibodies. WT retinæ show expected distribution of rhodopsin (RHO), transducin alpha (GNAT1) and CNGB1 (indicated by red color) whereas *Reep6*^{-/-} retinæ showed either reduced expression of GNAT1 and CNGB1; REEP6 immunostaining is indicated by green. (B) Immunoblot image of selected proteins in retinal extracts from 4-week old WT (+/+) and *Reep6*^{-/-} (-/-) mice, showing reduced expression of CNGB1, GARP, GNAT1 and AIPL1 in *Reep6*^{-/-} mice. Expression levels of rhodopsin and PDE do not appear to be altered in *Reep6*^{-/-} mice compared to the wild-type. β -Actin was used as a loading control.

middle panel showing OPL). At higher magnification, we detected co-localization of REEP6 (green) and Clathrin (red) to vesicles in rod spherules (Fig. 4F). The dark profile within each circular rod spherule represents a mitochondrion located near the ribbon synapse. REEP6 containing vesicles are also visible in the rod cytoplasm in the outer nuclear layer. A region of interest (ROI) comprised of rod spherules was analyzed to assess the extent of REEP6 and Clathrin co-localization. This region yielded a Pearson's correlation coefficient of 0.541 when calculated with Volocity co-localization software and utilizing auto-thresholding features. Over 50% value of correlation between REEP6 and Clathrin localization corroborates our biochemical studies demonstrating the presence of both Clathrin and REEP6 in a subset of Clathrin-coated membrane vesicles.

REEP6 interacts with STX3

To decipher how the vesicles marked with REEP6 are recognized at the destination, we analyzed molecules specifically involved in vesicle targeting, such as t-SNAREs (36). Mass spectrometry analysis revealed at least two STX3 peptides in two independent anti-REEP6 immunoprecipitated fractions from mouse retina, but not in the controls using IgG; thus, STX3 is a potential candidate t-SNARE for interacting with REEP6-marked vesicles. Notably, STX3 has been associated with trafficking of

membrane proteins in the mouse retina (37). Consistent with REEP6 localization (30) (Fig. 4E and F), STX3 is detected in the inner segments of photoreceptors and in outer plexiform layer (38). STX3 immunostaining was greatly reduced in photoreceptors of the *Reep6*^{-/-} retina (Fig. 5A). As predicted from the mass spectrometry data, STX3 could be immunoprecipitated with anti-REEP6 antibody from mouse retinal extracts (Fig. 5B), suggesting that REEP6 may potentially serve as a v-SNARE-like molecule for docking of specific Clathrin-coated vesicles by interacting with STX3.

Based on these observations, we propose that REEP6 is involved in vectorial transport of proteins in rod photoreceptors and that a subset of REEP6-marked Clathrin-coated vesicles delivers specific cargo to STX3-resident plasma membrane sites (Fig. 5C).

REEP6-E75K mutation is associated with retinitis pigmentosa

The preceding studies prompted us to examine REEP6 as a candidate gene for RP, which is commonly associated with rod dysfunction. Whole exome sequencing (WES) of retinopathy patients at two centers [National Eye Institute (NEI) and Wenzhou Medical University] identified two recessive RP families (one at each center) with a homozygous missense variant

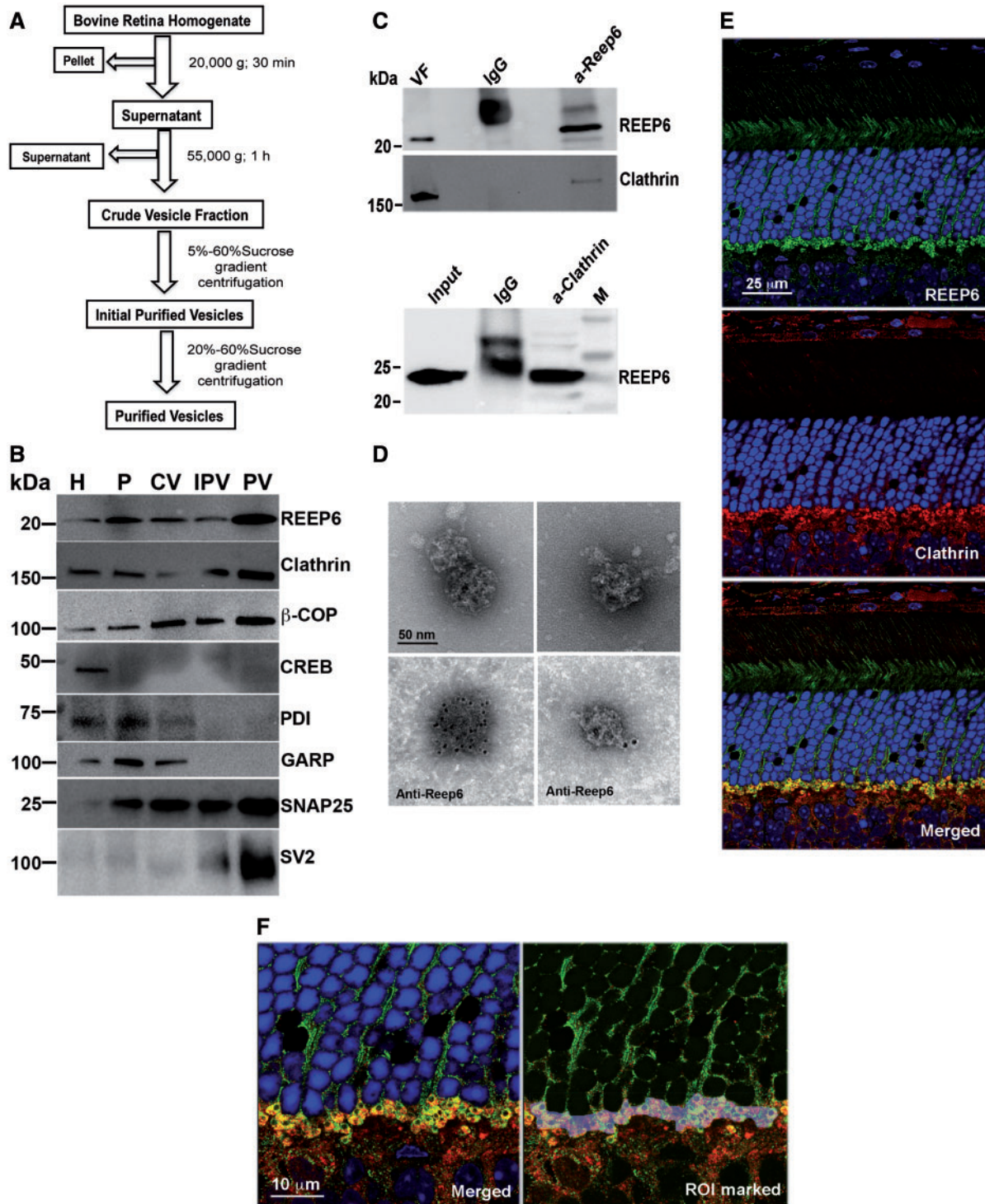


Figure 4. REEP6 is present in a subset of Clathrin-coated vesicles. (A) Schematic showing purification of vesicles from bovine retina. (B) Immunoblot image of fractions from bovine retinal homogenate (H), pellet (P), crude vesicles (CV), initial purification (IPV) and purified vesicles (PV) probed using antibodies against vesicular (Clathrin, COPI), membrane (SNAP25, SV2) and cytoplasmic (PDI, GARP) and nuclear (CREB) proteins. Note increased level of REEP6, Clathrin, β -COPI, SNAP-25 and SV2 in purified vesicles. CREB (a nuclear transcription factor) and PDI (an endoplasmic reticulum marker) are used as a negative control. GARP, an outer segment transmembrane protein, was not enriched in the purified vesicle. (C) Immunoblot showing co-IP of Clathrin and REEP6. Top panel shows immunoblot of proteins precipitated from purified vesicles with anti-REEP6 antibody and probed with anti-Clathrin. Bottom panel shows the reverse co-IP of mouse retinal extract using anti-Clathrin antibody to pull down REEP6. (D) EM and Immuno-EM images of Clathrin coated vesicles purified from bovine retina. The top panels show Clathrin-coated vesicles with the characteristic triskelion architecture. The bottom panels show anti-REEP6 conjugated nanogold particles bound to purified vesicles from bovine retina extract. (E) Co-localization images showing REEP6 (green) and Clathrin (Red) in adult mouse retina. Note that the green and red signals show strong localization in the plexiform layer in the rod spherules. (F) Higher magnification images of the plexiform layer showing a region of interest (ROI) selected for co-localization analysis; a Pearson coefficient of 0.541 was obtained using Volocity.

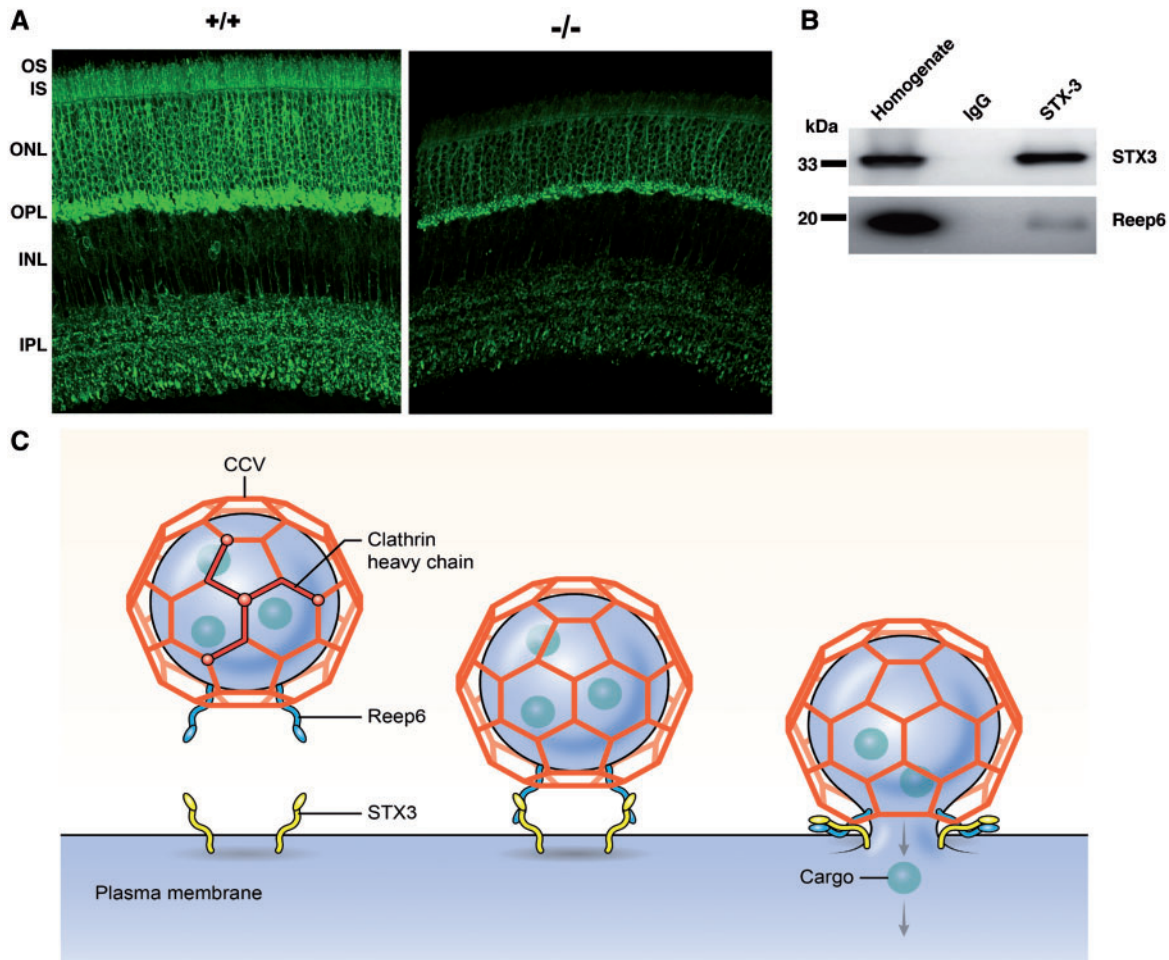


Figure 5. REEP6 interacts with STX3 in retina. (A) WT (+/+) and *Reep6*^{-/-} mouse retina stained with anti-STX3 and visualized with Alexa-Fluor 488 (green). STX3 signal is localized primarily in outer plexiform layer (OPL) and inner plexiform layer (IPL) but also in cell body and inner segment of photoreceptors in WT retina. In the *Reep6*^{-/-} mouse retina, STX3 signal intensity is reduced and is much less in inner segments of photoreceptors. (B) Proteins immunoprecipitated with anti-STX3 from mouse retina also showed REEP6 as an interacting partner as seen by the co-IP. (C) A model showing the presence of REEP6 on Clathrin-coated vesicle (CCV). REEP6 is shown interacting with CCV on the vesicle and docking with STX3 on the plasma membrane, resulting in membrane fusion and cargo release.

(NM_138393:exon 3: c.223G > A: p.E75K) in REEP6 (Fig. 6A and B). Sanger sequencing of the affected individual in both families and of two unaffected members from the American family confirmed the segregation (Fig. 6C). This variant was very rare in different populations (MAF = 0.00006654 in ExAC database: see Supplementary Materials, Table S4A and S4B for population-specific details).

The patient of African ethnicity (from the NEI cohort) noted night and side vision disturbances at age 8–9 years of age and was diagnosed with RP at the age of 30. Over the next decades, there was progressive vision loss (examined at Scheie Eye Institute). At age 52, visual acuities were 20/400, right eye and 20/40, left eye (no significant refractive errors). Intraocular pressures were normal (16 mm Hg) and there were minimal cataracts. Visual fields were restricted to a small central island in each eye. By age 73 years, visual acuities were 20/400, right eye, and hand motions vision, left eye. A central island of visual field was detectable in the right eye only. Fundus examination revealed dense pigmentary abnormalities consistent with the diagnosis of RP (Fig. 6D). No other family members had the diagnosis of RP or complaints suggesting retinal disease. The second patient was a male aged 46 years from a Han Chinese consanguineous family (first-cousins). All his family members were

unaffected. The proband was clinically diagnosed as typical RP in the Eye Hospital of the Wenzhou Medical University. He displayed severe visual impairment (visual acuities: HM in both eyes) and bone spicule-like pigment deposits in the fundus (Supplementary Material, Fig. S3). Previously, targeted exome sequencing had excluded known disease genes in this proband (39).

The c.223G > A, p.E75K variant was predicted to be pathogenic (Supplementary Material, Table S4C) and altered a highly conserved Glu75 residue. Structural modeling of the REEP6 protein revealed PFAM domain TB2_DP1_HVA22 (E-value: 1.5e–31, as determined by HMMER3) from residues 54 to 143 (Fig. 6E), which contain several linear motifs such as Class IV WW domain interaction motif that is recognized primarily by the Pin1 phosphorylation-dependent prolyl isomerase (residues 73–78), the substrate motif for phosphorylation by cytoplasmic cyclin-dependent protein kinase holoenzyme complex (residues 73–79), and proline-directed kinase phosphorylation site (residues 73–79). We suggest that functional importance of the TB2_DP1_HVA22 domain might be associated with phosphorylation of the ESPSK site. The E75K variant would result in the loss of helical conformation at the residue E75, capping one of the transmembrane helices (Fig. 6F), which could in turn

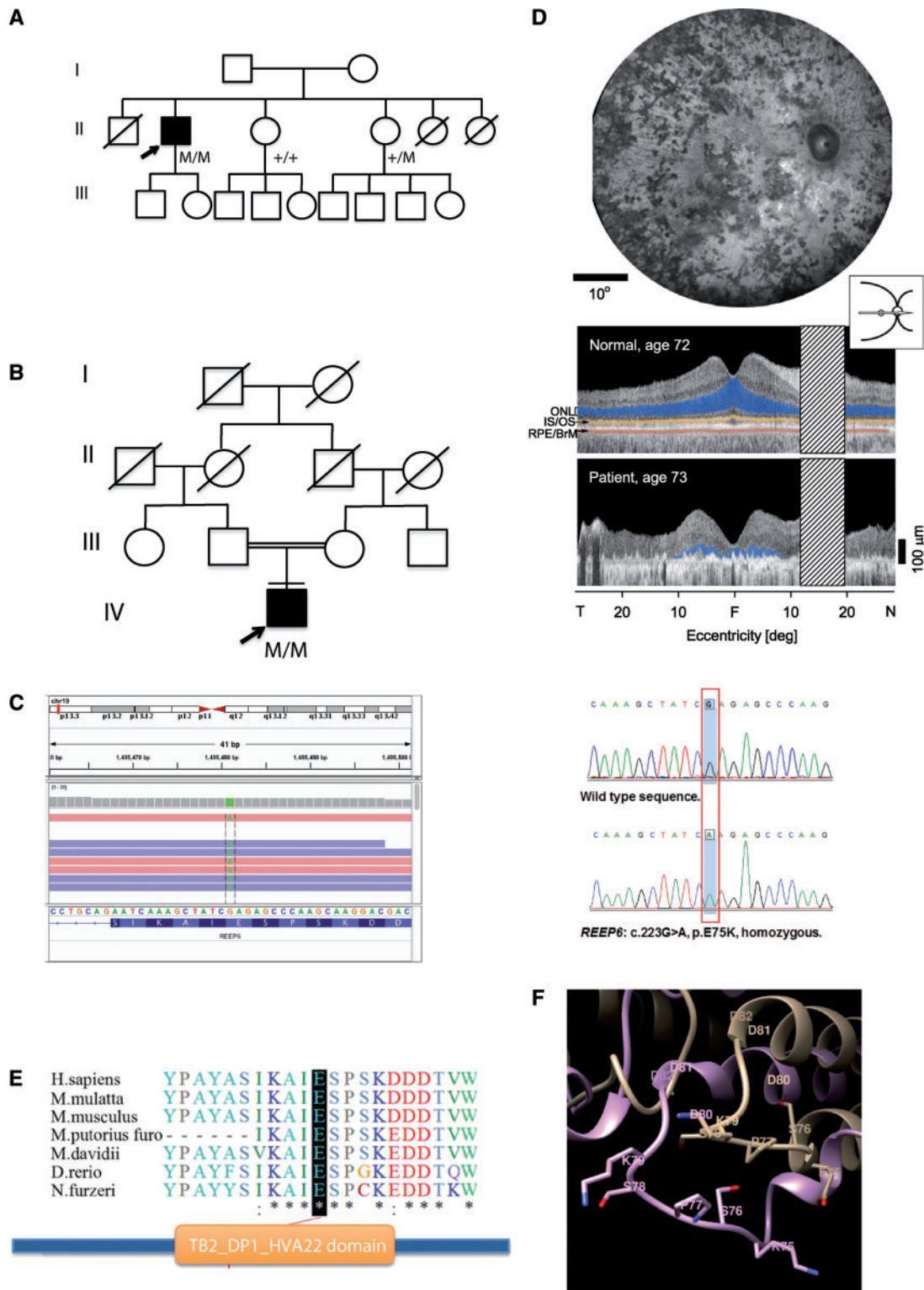


Figure 6. REEP6 mutation in patients with retinitis pigmentosa. (A, B) Pedigrees of two families with REEP6 mutation. Filled symbols designate affected individual and arrows indicate the proband. (C) IGV view showing exome sequencing reads and validating using Sanger sequencing with chromatograms showing WT (top) and homozygous (bottom) allele. (D) Phenotype of the RP patient (pedigree in 6A). *En face* fundus image shows pigmentary retinopathy (top). Cross-sectional imaging by optical coherence tomography in an age-related normal-sighted subject (top) and in the patient (bottom); laminae of the retina are highlighted in this section across the horizontal meridian. Photoreceptor or outer nuclear layer (ONL), blue; inner segment/outer segment (IS/OS) line, yellow; retinal pigment epithelium/Bruch's membrane (RPE/BrM), red. The RP patient has only limited ONL detectable and it is restricted to the central 20 degrees (deg), around the fovea; this relates to the severe loss of vision. T, temporal; N, nasal. Hatched bar, location of optic nerve. (E) Conservation of the E75 residue across different species and location in the REEP6 domain. (F) Homology modeling of the E75K mutation showing superposition of the PFAM domain TB2_DP1_HVA22 from the human REEP6 (shown in beige) and E75K mutant variant (shown in light blue) structures. Residues 73–79 are shown in orange (REEP6) and dark blue (E75K mutant). Side chains of potentially phosphorylated serine residue S76 are shown. Residue E75 is replaced with lysine K75 shown in red. The replacement disrupts charged interaction between E75 and K72, which results in a change of conformation of the loop including residues 73–79.

abrogate the specific docking motif required to activate the kinase enzymatic function.

Discussion

RP constitutes a heterogeneous group of inherited retinal diseases (IRDs) that are caused by mutation in 82 genes to date (<https://sph.uth.edu/retnet/>; date last accessed March 27, 2017). However, mutations in the reported genes can account for about 50% of IRDs (40–43), indicating involvement of additional genes. WES has now permitted the analysis of retinopathy families with even a single affected individual, without a priori knowledge of inheritance pattern, greatly expanding the repertoire of recessive genes. Here we report two patients of East Asian and African ethnicity with E75K variant as possible cause of RP. This variant is very rare and has been observed only in heterozygous state in apparently normal controls of East Asian and African descent. Additionally, WES of these patients revealed no other mutation in any reported retinal degeneration causing genes. The change causes a loss of helical conformation for the residue E75, capping one of the transmembrane helices, which we predict could cause a loss of the specific docking motif that is required to activate the kinase enzymatic function. Taken together, these results strongly argue in favor of the E75K in REEP6 being the causative mutation in the two families reported here.

While this manuscript was being submitted, REEP6 mutations were reported in five families with recessive RP (44); these mutations included three frameshift, two missense and one genomic rearrangement disrupting exon 1. While four families had frameshift deletion or duplication mutations, one family harbored a homozygous missense mutation, P128L. A knock-in of P128L mutation in mouse demonstrated significant thinning of outer nuclear layer and ERG dysfunction. One of the mutations specifically targets the novel REEP6 isoform we had reported, suggesting a critical function of this domain in rod photoreceptors. The reported studies are in concordance with the role of REEP6 in rod photoreceptors reported in our current study.

Rods and cones have distinct functions in mediating vision response and include many overlapping yet different components of phototransduction machinery. REEPs appear to have distinct functions in specific cell types, such as rod and cone photoreceptors. We hypothesize that the function of rod photoreceptor-specific REEP6 isoform at the synapse might be associated with neurotransmission kinetics. The vesicle release (rate of exocytosis) must be accelerated in cones 5–10 times compared with rods to achieve faster reaction kinetics (visual response) (45), which in turn would require SNARE molecules with differences in coupling modes during fusion reactions (46). Increasing the length of a SNARE is reported to progressively decrease the rate of coupling reaction, and thus topology is critical in determining the rate of membrane fusion (47). The kinetics of the scotopic ERG *b*-wave is slower in *Reep6*^{-/-} mice compared to the WT animals (data not shown), suggesting a potential defect in pre-/post-synaptic activity of rod rod-bipolar cells. Further investigations are required to examine the dynamics of neurotransmitter vesicle release/uptake in *Reep6*^{-/-} mice.

The canonical vesicles used for trafficking of specific cargo have additional built-in mechanisms to differentiate their contents. The vesicles marked with REEP6 may carry limited number of transmembrane proteins, such as CNGB1, as well as membrane-associated proteins such as GNAT1. Similar retinal degeneration phenotypes in *Cngb1*^{-/-} (48) and *Reep6*^{-/-} mice,

together with our biochemical results, suggest that CNGB1 is likely one of the cargos carried by the REEP6-marked Clathrin vesicles. It is unlikely that REEP6 is used for specifying the target because the cargo in REEP6-marked vesicles is likely docked by interaction with STX3, which may interact with other v-SNAREs as well. This is supported by the presence of STX3 in the inner plexiform layer of the retina in absence of REEP6 (38). Our data suggest that REEP6 is utilized for trafficking of proteins targeted to the rod plasma membrane. At an early age, we do observe altered scotopic ERG *b*-wave kinetics, which might reflect defects in synaptic transmission in the *Reep6*^{-/-} mice. A further decline was observed in late stage and might be secondary to degenerating photoreceptors.

REEP family of proteins, initially identified as partners of mammalian odorant receptors (23), are now established as membrane-shaping proteins involved in intracellular trafficking (24,26,27). Our studies strongly implicate REEP6 in marking a sub-population of Clathrin-coated vesicles for appropriate targeting of specific proteins to distinct membrane sites in rod photoreceptors. Given that REEP5 is more similar to REEP6 compared to *Reep1–4* (26), REEP5 may also be associated with membrane targeting during vesicle transport. Further investigations of REEP6-associated proteins should provide fundamental insights into cargo delivery to specific sites within the highly-polarized neurons, such as photoreceptors, and assist in developing strategies for treatment of associated neurodegenerative diseases.

Materials and Methods

Generation and characterization of *Reep6*^{-/-} mice

All mouse experiments were conducted after approval from Animal Care and Use Committee of the NEI. *Reep6*^{-/-} germline mice were generated by homologous recombination in R1 ES cells (Fig. 1), as described (49), and bred into C57BL/6J mice (Jackson Laboratory, Bar Harbor). Scotopic and photopic ERGs were performed in mice as previously described (50).

Immunoblot analysis

Mouse retina was dissected out and the tissues were lysed by homogenization in radioimmunoprecipitation assay (RIPA) buffer supplemented with N-ethylmaleimide and protease inhibitor mixture (Roche Applied Science). The protein concentration in the lysate was measured by the bicinchoninic acid assay (Thermo Scientific) and equal amounts of lysates were subjected to SDS-PAGE analysis. The membrane was probed sequentially with primary antibodies and horseradish peroxidase tagged secondary antibodies and visualized by enhanced chemiluminescence (Thermo Scientific).

Histology and immunofluorescence microscopy

Eyes from wild type and *Reep6*^{-/-} mice (at age 1, 3 and 6 month, and 1 or 2 year) were fixed with 4% glutaraldehyde for 30 min at room temperature and then with 4% paraformaldehyde overnight at 4°C. After washing with PBS, eyes were embedded in plastic or paraffin, and 10 μm sections were cut and stained with standard H&E staining protocol.

Eyes from P30 WT and *Reep6*^{-/-} mice were fixed in 4% paraformaldehyde for 30 min. The retinas were dissected and sectioned at 150 μm on a Vibratome. Immunofluorescent staining was performed as described (31), using the following primary

antibodies: a custom rabbit polyclonal antibody to REEP6 [1:1000 (30,31)], a mouse monoclonal antibody to Rhodopsin, (1:2000; Dr. Tiansen Li, NEI), a mouse monoclonal antibody to Transducin alpha, (1:2000; Dr. Tiansen Li, NEI), a mouse monoclonal hybridoma supernatant antibody to CNGB-N terminal, (GARP 4B1, 1:10; Dr. Robert Molday, Vancouver, Canada) (51). Secondary antibodies raised in donkey to either rabbit or mouse IgG and conjugated to AlexaFluor dyes (1:200; Life Technologies) were used to detect the primary antibodies. Retinal sections were imaged using an Olympus FluoView FV1000 confocal laser scanner and processed in Adobe Photoshop CS3 to adjust contrast.

Gene expression analysis

Total RNA was isolated from C57BL/6J mouse and *Reep6*^{-/-} retina using TRIzol reagent (Invitrogen), and cDNA was synthesized using the Superscript II QPCR cDNA Synthesis Kit (Thermo Fisher Scientific). Gene expression was detected by qPCR using Taqman probes (IDs: Mm01170350_g1, Mm01173489_m1, Mm01315649_m1) and 2X-Gene Expression Master mix (Applied Biosystems).

RNA sequencing and analysis

Directional RNA-seq library construction and sequencing was performed as previously described (52). Briefly, 1 µg of total RNA was used for library construction. Each library was single-end sequenced in an independent lane of a GAIIx (Illumina, Inc.) at a length of 76 bases (53). Fastq files were generated from reads passing chastity filter and used for further analysis.

Transcript level quantitation was performed using kallisto v0.42.4 (54) employing a merged transcript cDNA and ncRNA FASTA file downloaded from the Ensembl ftp site for v84 assembly. All secondary analyses were performed in the R statistical environment (www.r-project.org; date last accessed March 27, 2017). Normalized reads per kilobase of exon model per million reads (RPKM) values were obtained using TMM normalization in edgeR v3.13.9 (55,56). Gene level quantification was generated by summarization of the transcript level quantitation using tximport v0.99.9 (57) with the option 'countFromAbundance = lengthScaledTPM'. The gene level count values were TMM normalized and converted to count per million (CPM) via edgeR. Principal component analysis was accomplished with normalized log₂ CPM values. PCA analyses were visualized with the pca3d v0.8 package. Differential expression analysis on genes having greater than 1 CPM for all replicates of any genotype was performed at the gene level using limma v3.27.19 (58). P9 and P21 were filtered for expression and analyzed separately. Dispersion estimation was performed with the voom function and contrast statistics employed with the eBayes function by specifying all coefficients for analysis. Genes having greater than two-fold change and FDR of <5% in any comparison were used for further analysis. Hierarchical clustering was performed on the significantly differentially expressed genes identified from the limma analysis. Ward method using Euclidean distance was performed on the log₂ CPM. Gene ontology and Kegg pathway enrichment analysis was performed using limma. To reduce redundancy associated with GO analysis, we selected only ontologies having an enriched term <0.01 FDR and representation using the most end-of-branch term.

Purification and analysis of vesicles

Coated vesicles were purified from homogenates of 40 bovine retinæ as described (59). All steps were performed at 4 °C. Briefly, the retinæ were suspended with equal volume of 2X homogenization buffer (0.1M morpholino ethane sulphonic acid pH6.5, 1mM EGTA, 0.5 mM MgCl₂) homogenized with a Teflon glass homogenizer and then centrifuged at 20,000 x g for 30 min. The supernatant was centrifuged at 55,000g for 1 h. The resulting pellet contained crude vesicles (CV). The pellet was suspended in 1 ml of homogenization buffer and layered on top of 12 ml continuous 5%–60% sucrose gradient and centrifuged for 2 h at 50,000g. The gradient was fractionated and the milky white band in the middle was collected (Initial Purified Vesicles). This vesicle fraction was diluted four times with the buffer and pelleted by centrifugation at 100,000g for 1 h. The pellet was suspended in 0.5 ml of buffer and layered on top of a 20%–60% sucrose gradient and centrifuged for 16 h at 50,000g. The turbid band around 55% sucrose was collected and concentrated to yield purified vesicles.

The vesicles were placed on a glow-discharged carbon coated Formvar-film grid, excess solution was removed by blotting, and the grids were air dried. Then, 5 µl uranyl acetate solution (1% w/v aqueous solution) was added to the grid, excess solution was removed by repeated blotting. After air dry, the grids were examined and imaged with an electron microscope (H7650, Hitachi) at 80 kV. For immuno-EM, a drop of anti-REEP6 antibody (1/25 dilution) was added for 1 h to vesicles attached on the Formvar-carbon coated grids. The grids were washed in TBS [50mM Tris buffer containing 125 mM NaCl, 0.1% BSA (w/v)] three times for 10 min each, and then incubated in gold-conjugated secondary antibody for 1 h, followed by TBS washing. Finally, the grids were negatively stained in uranyl acetate (0.5% w/v) aqueous solution and examined by EM.

Electron microscopy

P17 retina was fixed in paraformaldehyde (4% v/v) and glutaraldehyde (2% v/v) in cacodylate buffer (0.1 M, pH7.4) for 2 h at room temperature and then washed in cacodylate buffer thrice (10 min each). The retina was then treated for 1 h in osmium tetroxide (1% v/v), washed thrice (10 min each) in cacodylate buffer, then washed once in acetate buffer (0.1 M pH 4.2) (Electron Microscope Science) and stained in acetate buffer containing 0.1% (w/v) uranyl acetate (Electron Microscope Science) for 1 h. The sample was dehydrated in a series of ethanol (e.g. 35%, 50%, 75%, 95%, and 100%) and in propylene oxide. The retinas were infiltrated in a mixture of propylene oxide and epoxy resin (1:1) overnight on a rotating table and embedded in a pure epoxy resin at 55 °C for 48 h. Thin sections (80–90 nm) were cut and mounted on copper grids and stained in uranyl acetate and lead citrate. The sections were stabilized by carbon evaporation prior to examination and imaged in the electron microscope (Hitachi H7650).

Co-localization of REEP6 and clathrin in mouse retina

REEP6 and Clathrin co-localization studies were performed using C57BL/6 wild type adult mouse eyes. Following 2-h fixation in 4% paraformaldehyde in 1× PBS, eyes were washed and dissected. Posterior cups were embedded in agarose and sectioned on a VT1000 vibrating microtome (Leica Microsystems) (60). Thick sections (100 µm) were incubated in antibodies to REEP6 (rabbit) and Clathrin (goat) overnight. Following repeated

washing in immunohistochemistry buffer, sections were incubated for 4 h in fluorescently conjugated secondary antibodies (donkey anti-rabbit Alexa 488 and Donkey anti-goat Alexa 568, from Invitrogen). DAPI was included as a nuclear marker. Following repeated washing, sections were transferred to slides, cover-slipped and imaged on a Zeiss LSM 880 Airyscan imaging system operating with Zen 2.1 (Carl Zeiss Imaging). High resolution Airy Scan images were collected with a 63×1.4 NA oil immersion objective. Individual channels were collected sequentially at Nyquist conditions as 16 bit/channel files using 32-element Airy detector. All laser and detector settings were standardized for both experimental and negative controls.

Co-localization analysis was performed with Velocity ver. 6.3.0 (Perkin Elmer). An auto-thresholding feature within this program (61) was applied to images. A region of interest (ROI) encompassing rod spherules in the outer plexiform layer was drawn, and a Pearson's correlation coefficient was calculated for this ROI.

Patient characterization and mutation analysis

Informed consent was obtained from the subjects. The Institutional Review Board approved protocols for study of the U.S. family; and the procedures adhered to the tenets of the Declaration of Helsinki. The Ethics committee of the Eye Hospital of the Wenzhou Medical University approved studies on Chinese family. Genomic DNA samples were quantified using the QuantiFluor® dsDNA system (Promega) and whole exome sequencing was performed according to manufacturer's instructions. Briefly, enrichment of the DNA libraries was carried out using the Exome Enrichment V5 Kit (Agilent Technologies) or Nextera Rapid Capture Expanded Exome kit (Illumina) according to the manufacturers' protocol. Whole-exome-enriched DNA libraries were sequenced on a HiSeq 2000 sequencer (Illumina). FastQC was used to confirm quality of sequencing. Adapter indexes were removed using Trimmomatic, and sequence reads were mapped to the human reference sequence (hg19, GRCH37) using BWA (62). Single-nucleotide variants (SNVs) and insertion-deletion variants (InDels) were called using GATK (63) and ANNOVAR was used for annotations (64). Variants with minor allele frequency (MAF) of >0.005 in any of the variant databases, including Exome Aggregation Consortium (ExAC, <http://exac.broadinstitute.org/>; date last accessed March 27, 2017), 1000 Genome (www.1000genomes.org; date last accessed March 27, 2017), dbSNP137 (www.ncbi.nlm.nih.gov/SNP/; date last accessed March 27, 2017) and NHLBI Exome Sequencing Project (ESP, <http://evs.gs.washington.edu/EVS/>; date last accessed March 27, 2017) were filtered. The damage predictions of variants were based on 14 different software and CADD scores. Variants predicted as damaging in more than eight tools were included in the process. Sanger validation was carried out to exclude the false-positive variants.

Protein modeling

The amino acid sequence of human REEP6 (isoform 1) was retrieved from the NCBI (Reference # NP_001316485.1). Homology modeling of REEP6 protein structure was performed using RaptorX structure prediction web-server (<http://raptorx.uchicago.edu/>; date last accessed March 27, 2017) with using the protein structure of the reduced form of cytochrome ba3 oxidase as the structural template (RDB: 3eh3 A, P -value $3.22e^{-03}$). In total, 211 residues were modeled in the REEP6 structure, including 43

residues at the C-terminus predicted to be disordered. Subdomain identification was performed using Simple Modular Research Tool, SMART (smart.embl-heidelberg.de) and functional sites were determined by the ELM motif search (<http://elm.eu.org/>; date last accessed March 27, 2017).

Author contributions

Overall Conceptualization, S.V. and A.S.; Methodology and Investigation, S.V., S.H.M., J.N., B.M.; Resource Generation (knockout mouse), L.D.; ERG analysis, H.Q., S.V.; Cell Biology, S.V., S.H.M, R.F., T.L.; EM, K.N., C.G., R.F.; RNA-seq, M.J.B.; Patient Characterization and Whole exome analysis, S.G.J, A.V.C., R.R., X.-F.H., J.Q., F.L., Z.-B.J.; Structure modeling, Y.S.; Writing—Original Draft, S.V., A.S.; Writing—Review & Editing, S.V., J.N., R. R., A.V.C., Z.-B.J., S.G.J. and A.S.; Funding Acquisition, A.S., S.G.J., Z.-B.J.; Supervision and Project Administration, A.S.

Supplementary Material

Supplementary Material is available at HMG online.

Acknowledgements

We are grateful to David Sherry for anti-STX3 antibody and thank Linn Gieser and Ashrithpal P. Reddy for assistance with WES.

Conflict of Interest statement. None declared.

Funding

This research was supported by Intramural Research Program (EY000450, EY000546) of the National Eye Institute, and the National Key Basic Research Program (2013CB967502, to ZB), National Natural Science Foundation of China (81371059, 81522014, to ZB). WES data analysis utilized computational resources of the NIH HPC Biowulf cluster (<https://hpc.nih.gov/>; date last accessed March 27, 2017). This project was also supported in part with federal funds from the National Cancer Institute, under contract HHSN26120080001E. The content of this publication does not necessarily reflect the views or policies of the Department of Health and Human Services, nor does mention of trade names, commercial products, or organizations imply endorsement by the U.S. Government. Funding to pay the Open Access publication charges for this article was provided by intramural research program of the National Eye Institute.

References

- Lamb, T.D. (2013) Evolution of phototransduction, vertebrate photoreceptors and retina. *Prog. Retin. Eye Res.*, **36**, 52–119.
- Hoon, M., Okawa, H., Della Santina, L. and Wong, R.O. (2014) Functional architecture of the retina: development and disease. *Prog. Retin. Eye Res.*, **42**, 44–84.
- Okawa, H., Sampath, A.P., Laughlin, S.B. and Fain, G.L. (2008) ATP consumption by mammalian rod photoreceptors in darkness and in light. *Curr. Biol.*, **18**, 1917–1921.
- Kim, J.W., Yang, H.J., Oel, A.P., Brooks, M.J., Jia, L., Plachetzki, D.C., Li, W., Allison, W.T. and Swaroop, A. (2016) Recruitment of rod photoreceptors from short-wavelength-sensitive cones during the evolution of nocturnal vision in mammals. *Dev. Cell*, **37**, 520–532.

5. Curcio, C.A., Sloan, K.R., Kalina, R.E. and Hendrickson, A.E. (1990) Human photoreceptor topography. *J. Comp. Neurol.*, **292**, 497–523.
6. Wright, A.F., Chakarova, C.F., Abd El-Aziz, M.M. and Bhattacharya, S.S. (2010) Photoreceptor degeneration: genetic and mechanistic dissection of a complex trait. *Nat. Rev. Genet.*, **11**, 273–284.
7. Fritsche, L.G., Fariss, R.N., Stambolian, D., Abecasis, G.R., Curcio, C.A. and Swaroop, A. (2014) Age-related macular degeneration: genetics and biology coming together. *Annu. Rev. Genomics Hum. Genet.*, **15**, 151–171.
8. Young, R.W. (1969) A difference between rods and cones in the renewal of outer segment protein. *Invest. Ophthalmol.*, **8**, 222–231.
9. Goldberg, A.F., Moritz, O.L. and Williams, D.S. (2016) Molecular basis for photoreceptor outer segment architecture. *Prog. Retin. Eye Res.*, **55**, 52–81.
10. Abd-El-Barr, M.M., Sykoudis, K., Andrabi, S., Eichers, E.R., Pennesi, M.E., Tan, P.L., Wilson, J.H., Katsanis, N., Lupski, J.R. and Wu, S.M. (2007) Impaired photoreceptor protein transport and synaptic transmission in a mouse model of Bardet-Biedl syndrome. *Vision Res.*, **47**, 3394–3407.
11. Pazour, G.J. and Bloodgood, R.A. (2008) Targeting proteins to the ciliary membrane. *Curr. Top. Dev. Biol.*, **85**, 115–149.
12. Lopes, V.S., Jimeno, D., Khanobdee, K., Song, X., Chen, B., Nusinowitz, S. and Williams, D.S. (2010) Dysfunction of heterotrimeric kinesin-2 in rod photoreceptor cells and the role of opsin mislocalization in rapid cell death. *Mol. Biol. Cell*, **21**, 4076–4088.
13. Nishiwaki, Y., Yoshizawa, A., Kojima, Y., Oguri, E., Nakamura, S., Suzuki, S., Yuasa-Kawada, J., Kinoshita-Kawada, M., Mochizuki, T. and Masai, I. (2013) The BH3-only SNARE BNip1 mediates photoreceptor apoptosis in response to vesicular fusion defects. *Dev. Cell*, **25**, 374–387.
14. Nagel-Wolfrum, K. and Wolfrum, U. (2013) Vesicle transport and photoreceptor death: fishing for molecular links. *Dev. Cell*, **25**, 435–436.
15. Rosenbaum, E.E., Vasiljevic, E., Cleland, S.C., Flores, C. and Colley, N.J. (2014) The Gos28 SNARE protein mediates intracellular transport of rhodopsin and is required for photoreceptor survival. *J. Biol. Chem.*, **289**, 32392–32409.
16. Wang, J. and Deretic, D. (2014) Molecular complexes that direct rhodopsin transport to primary cilia. *Prog. Retin. Eye Res.*, **38**, 1–19.
17. Wensel, T.G., Zhang, Z., Anastassov, I.A., Gilliam, J.C., He, F., Schmid, M.F. and Robichaux, M.A. (2016) Structural and molecular bases of rod photoreceptor morphogenesis and disease. *Prog. Retin. Eye Res.*, **55**, 32–51.
18. Faini, M., Beck, R., Wieland, F.T. and Briggs, J.A. (2013) Vesicle coats: structure, function, and general principles of assembly. *Trends Cell Biol.*, **23**, 279–288.
19. Mohrmann, R. and Sorensen, J.B. (2012) SNARE requirements en route to exocytosis: from many to few. *J. Mol. Neurosci.*, **48**, 387–394.
20. Ramakrishnan, N.A., Drescher, M.J. and Drescher, D.G. (2012) The SNARE complex in neuronal and sensory cells. *Mol. Cell Neurosci.*, **50**, 58–69.
21. Fang, Q. and Lindau, M. (2014) How could SNARE proteins open a fusion pore? *Physiology (Bethesda)*, **29**, 278–285.
22. Hong, W. and Lev, S. (2014) Tethering the assembly of SNARE complexes. *Trends Cell Biol.*, **24**, 35–43.
23. Saito, H., Kubota, M., Roberts, R.W., Chi, Q. and Matsunami, H. (2004) RTP family members induce functional expression of mammalian odorant receptors. *Cell*, **119**, 679–691.
24. Bjork, S., Hurt, C.M., Ho, V.K. and Angelotti, T. (2013) REEPs are membrane shaping adapter proteins that modulate specific G protein-coupled receptor trafficking by affecting ER cargo capacity. *PLoS One*, **8**, e76366.
25. Zuchner, S., Wang, G., Tran-Viet, K.N., Nance, M.A., Gaskell, P.C., Vance, J.M., Ashley-Koch, A.E. and Pericak-Vance, M.A. (2006) Mutations in the novel mitochondrial protein REEP1 cause hereditary spastic paraplegia type 31. *Am. J. Hum. Genet.*, **79**, 365–369.
26. Park, S.H., Zhu, P.P., Parker, R.L. and Blackstone, C. (2010) Hereditary spastic paraplegia proteins REEP1, spastin, and atlastin-1 coordinate microtubule interactions with the tubular ER network. *J. Clin. Invest.*, **120**, 1097–1110.
27. Hu, J., Shibata, Y., Zhu, P.P., Voss, C., Rismanchi, N., Prinz, W.A., Rapoport, T.A. and Blackstone, C. (2009) A class of dynamin-like GTPases involved in the generation of the tubular ER network. *Cell*, **138**, 549–561.
28. Hu, J., Prinz, W.A. and Rapoport, T.A. (2011) Weaving the web of ER tubules. *Cell*, **147**, 1226–1231.
29. Schlaitz, A.L., Thompson, J., Wong, C.C., Yates, J.R., 3rd. and Heald, R. (2013) REEP3/4 ensure endoplasmic reticulum clearance from metaphase chromatin and proper nuclear envelope architecture. *Dev. Cell*, **26**, 315–323.
30. Keeley, P.W., Luna, G., Fariss, R.N., Skyles, K.A., Madsen, N.R., Raven, M.A., Poche, R.A., Swindell, E.C., Jamrich, M., Oh, E.C., et al. (2013) Development and plasticity of outer retinal circuitry following genetic removal of horizontal cells. *J. Neurosci.*, **33**, 17847–17862.
31. Hao, H., Veleri, S., Sun, B., Kim, D.S., Keeley, P.W., Kim, J.W., Yang, H.J., Yadav, S.P., Manjunath, S.H., Sood, R., et al. (2014) Regulation of a novel isoform of receptor expression enhancing protein REEP6 in rod photoreceptors by bZIP transcription factor NRL. *Hum. Mol. Genet.*, **23**, 4260–4271.
32. Swaroop, A., Kim, D. and Forrest, D. (2010) Transcriptional regulation of photoreceptor development and homeostasis in the mammalian retina. *Nat. Rev. Neurosci.*, **11**, 563–576.
33. Weymouth, A.E. and Vingrys, A.J. (2008) Rodent electroretinography: methods for extraction and interpretation of rod and cone responses. *Prog. Retin. Eye Res.*, **27**, 1–44.
34. Hagstrom, S.A., Duyao, M., North, M.A. and Li, T. (1999) Retinal degeneration in *tulp1*^{-/-} mice: vesicular accumulation in the interphotoreceptor matrix. *Invest. Ophthalmol. Vis. Sci.*, **40**, 2795–2802.
35. Lobanova, E.S., Finkelstein, S., Skiba, N.P. and Arshavsky, V.Y. (2013) Proteasome overload is a common stress factor in multiple forms of inherited retinal degeneration. *Proc. Natl. Acad. Sci. U S A*, **110**, 9986–9991.
36. Pfeffer, S.R. (1999) Transport-vesicle targeting: tethers before SNAREs. *Nat. Cell Biol.*, **1**, E17–E22.
37. Curtis, L.B., Doneske, B., Liu, X., Thaller, C., McNew, J.A. and Janz, R. (2008) Syntaxin 3b is a t-SNARE specific for ribbon synapses of the retina. *J. Comp. Neurol.*, **510**, 550–559.
38. Sherry, D.M., Mitchell, R., Standifer, K.M. and du Plessis, B. (2006) Distribution of plasma membrane-associated syntaxins 1 through 4 indicates distinct trafficking functions in the synaptic layers of the mouse retina. *BMC Neurosci.*, **7**, 54.
39. Huang, X.F., Huang, F., Wu, K.C., Wu, J., Chen, J., Pang, C.P., Lu, F., Qu, J. and Jin, Z.B. (2015) Genotype-phenotype correlation and mutation spectrum in a large cohort of patients

- with inherited retinal dystrophy revealed by next-generation sequencing. *Genet. Med.*, **17**, 271–278.
40. Zhao, L., Wang, F., Wang, H., Li, Y., Alexander, S., Wang, K., Willoughby, C.E., Zaneveld, J.E., Jiang, L., Soens, Z.T., et al. (2015) Next-generation sequencing-based molecular diagnosis of 82 retinitis pigmentosa probands from Northern Ireland. *Hum. Genet.*, **134**, 217–230.
 41. Koboldt, D.C., Larson, D.E., Sullivan, L.S., Bowne, S.J., Steinberg, K.M., Churchill, J.D., Buhr, A.C., Nutter, N., Pierce, E.A., Blanton, S.H., et al. (2014) Exome-based mapping and variant prioritization for inherited Mendelian disorders. *Am. J. Hum. Genet.*, **94**, 373–384.
 42. Consugar, M.B., Navarro-Gomez, D., Place, E.M., Bujakowska, K.M., Sousa, M.E., Fonseca-Kelly, Z.D., Taub, D.G., Janessian, M., Wang, D.Y., Au, E.D., et al. (2015) Panel-based genetic diagnostic testing for inherited eye diseases is highly accurate and reproducible, and more sensitive for variant detection, than exome sequencing. *Genet. Med.*, **17**, 253–261.
 43. Ellingford, J.M., Barton, S., Bhaskar, S., Williams, S.G., Sergouniotis, P.I., O'Sullivan, J., Lamb, J.A., Perveen, R., Hall, G., Newman, W.G., et al. (2016) Whole genome sequencing increases molecular diagnostic yield compared with current diagnostic testing for inherited retinal disease. *Ophthalmology*, **123**, 1143–1150.
 44. Arno, G., Agrawal, S.A., Eblimit, A., Bellingham, J., Xu, M., Wang, F., Chakarova, C., Parfitt, D.A., Lane, A., Burgoyne, T., et al. (2016) Mutations in REEP6 cause autosomal-recessive retinitis pigmentosa. *Am. J. Hum. Genet.*, **99**, 1305–1315.
 45. Rabl, K., Cadetti, L. and Thoreson, W.B. (2005) Kinetics of exocytosis is faster in cones than in rods. *J. Neurosci.*, **25**, 4633–4640.
 46. Hernandez, J.M., Kreutzberger, A.J., Kiessling, V., Tamm, L.K. and Jahn, R. (2014) Variable cooperativity in SNARE-mediated membrane fusion. *Proc. Natl. Acad. Sci. U S A*, **111**, 12037–12042.
 47. McNew, J.A., Weber, T., Engelman, D.M., Sollner, T.H. and Rothman, J.E. (1999) The length of the flexible SNAREpin juxtaposition region is a critical determinant of SNARE-dependent fusion. *Mol. Cell*, **4**, 415–421.
 48. Huttel, S., Michalakakis, S., Seeliger, M., Luo, D.G., Acar, N., Geiger, H., Hudl, K., Mader, R., Haverkamp, S., Moser, M., et al. (2005) Impaired channel targeting and retinal degeneration in mice lacking the cyclic nucleotide-gated channel subunit CNGB1. *J. Neurosci.*, **25**, 130–138.
 49. Thomas, K.R. and Capecchi, M.R. (1987) Site-directed mutagenesis by gene targeting in mouse embryo-derived stem cells. *Cell*, **51**, 503–512.
 50. Pang, J.J., Chang, B., Hawes, N.L., Hurd, R.E., Davisson, M.T., Li, J., Noorwez, S.M., Malhotra, R., McDowell, J.H., Kaushal, S., et al. (2005) Retinal degeneration 12 (rd12): a new, spontaneously arising mouse model for human Leber congenital amaurosis (LCA). *Mol. Vis.*, **11**, 152–162.
 51. Poetsch, A., Molday, L.L. and Molday, R.S. (2001) The cGMP-gated channel and related glutamic acid-rich proteins interact with peripherin-2 at the rim region of rod photoreceptor disc membranes. *J. Biol. Chem.*, **276**, 48009–48016.
 52. Brooks, M.J., Rajasimha, H.K. and Swaroop, A. (2012) Retinal transcriptome profiling by directional next-generation sequencing using 100 ng of total RNA. *Methods Mol. Biol.*, **884**, 319–334.
 53. Brooks, M.J., Rajasimha, H.K., Roger, J.E. and Swaroop, A. (2011) Next-generation sequencing facilitates quantitative analysis of wild-type and Nrl(-/-) retinal transcriptomes. *Mol. Vis.*, **17**, 3034–3054.
 54. Bray, N.L., Pimentel, H., Melsted, P. and Pachter, L. (2016) Near-optimal probabilistic RNA-seq quantification. *Nat. Biotechnol.*, **34**, 525–527.
 55. Robinson, M.D., McCarthy, D.J. and Smyth, G.K. (2010) edgeR: a Bioconductor package for differential expression analysis of digital gene expression data. *Bioinformatics*, **26**, 139–140.
 56. Robinson, M.D. and Oshlack, A. (2010) A scaling normalization method for differential expression analysis of RNA-seq data. *Genome Biol.*, **11**, R25.
 57. Sonesson, C., Love, M.I. and Robinson, M.D. (2015) Differential analyses for RNA-seq: transcript-level estimates improve gene-level inferences. *F1000Res*, **4**, 1521.
 58. Law, C.W., Chen, Y., Shi, W. and Smyth, G.K. (2014) voom: Precision weights unlock linear model analysis tools for RNA-seq read counts. *Genome Biol.*, **15**, R29.
 59. Pearse, B.M. (1975) Coated vesicles from pig brain: purification and biochemical characterization. *J. Mol. Biol.*, **97**, 93–98.
 60. Hale, I.L. and Matsumoto, B. (2002) Resolution of subcellular detail in thick tissue sections: immunohistochemical preparation and fluorescence confocal microscopy. *Methods Cell Biol.*, **70**, 301–335.
 61. Costes, S.V., Daelemans, D., Cho, E.H., Dobbin, Z., Pavlakis, G. and Lockett, S. (2004) Automatic and quantitative measurement of protein-protein colocalization in live cells. *Biophys. J.*, **86**, 3993–4003.
 62. Li, H. and Durbin, R. (2010) Fast and accurate long-read alignment with Burrows-Wheeler transform. *Bioinformatics*, **26**, 589–595.
 63. McKenna, A., Hanna, M., Banks, E., Sivachenko, A., Cibulskis, K., Kernytsky, A., Garimella, K., Altshuler, D., Gabriel, S., Daly, M., et al. (2010) The Genome Analysis Toolkit: a MapReduce framework for analyzing next-generation DNA sequencing data. *Genome Res.*, **20**, 1297–1303.
 64. Wang, K., Li, M. and Hakonarson, H. (2010) ANNOVAR: functional annotation of genetic variants from high-throughput sequencing data. *Nucleic Acids Res.*, **38**, e164.